AGU PUBLICATIONS

Geophysical Research Letters

RESEARCH LETTER
10.1002/2016GL070934

Special Section:
First results from NASA's Magnetospheric Multiscale (MMS) Mission

The substructure of a flux transfer event observed by the MMS spacecraft

K.-J. Hwang[1,2], D. G. Sibeck[1], B. L. Giles[1], C. J. Pollock[3], D. Gershman[1], L. Avanov[1], W. R. Paterson[1], J. C. Dorelli[1], R. E. Ergun[4], C. T. Russell[5], R. J. Strangeway[5], B. Mauk[6], I. J. Cohen[6], R. B. Torbert[7], and J. L. Burch[8]

[1]NASA Goddard Space Flight Center, Greenbelt, Maryland, USA, [2]The Goddard Planetary Heliophysics Institute, University of Maryland, Baltimore County, Baltimore, Maryland, USA, [3]Denali Scientific, LLC, Healy, Alaska, USA, [4]Laboratory for Atmospheric and Space Physics, University of Colorado Boulder, Boulder, Colorado, USA, [5]Institute of Geophysics and Planetary Physics, University of California, Los Angeles, California, USA, [6]The Johns Hopkins University Applied Physics Laboratory, Laurel, Maryland, USA, [7]Space Science Center, University of New Hampshire, Durham, New Hampshire, USA, [8]Southwest Research Institute, San Antonio, Texas, USA

Key Points:
- Multilayers of open and draped fields in and around the FTE exhibit rapid-varying connectivities to the magnetosphere and the FTE
- The interface between the core and draped regions contains a separatrix of newly opened magnetic field lines
- D-shaped ion distributions feature the axis of flux ropes that carry old-opened field lines

Correspondence to:
K.-J. Hwang,
kyoung-joo.hwang@nasa.gov

Citation:
Hwang, K.-J., et al. (2016), The substructure of a flux transfer event observed by the MMS spacecraft, *Geophys. Res. Lett.*, *43*, 9434–9443, doi:10.1002/2016GL070934.

Received 23 AUG 2016
Accepted 6 SEP 2016
Accepted article online 9 SEP 2016
Published online 23 SEP 2016

Abstract On 15 August 2015, MMS (Magnetospheric Multiscale mission), skimming the dusk magnetopause, detected an isolated region of an increased magnetic strength and bipolar B_n, indicating a flux transfer event (FTE). The four spacecraft in a tetrahedron allowed for investigations of the shape and motion of the FTE. In particular, high-resolution particle data facilitated our exploration of FTE substructures and their magnetic connectivity inside and surrounding the FTE. Combined field and plasma observations suggest that the core fields are open, magnetically connected to the northern magnetosphere from which high-energy particles leak; ion "D" distributions characterize the axis of flux ropes that carry old-opened field lines; counterstreaming electrons superposed by parallel-heated components populate the periphery surrounding the FTE; and the interface between the core and draped regions contains a separatrix of newly opened magnetic field lines that emanate from the X line above the FTE.

1. Introduction

Flux transfer event(s), FTE(s), are defined as a single transient structure or a series of bipolar signatures in the magnetic field component normal to the nominal magnetopause (B_n). Since *Russell and Elphic* [1978] who first discovered FTEs using the data from the ISEE spacecraft, their statistical properties have been widely studied [e.g., *Paschmann et al.*, 1982; *Sibeck and Siscoe*, 1984; *Southwood et al.*, 1986; *Kawano et al.*, 1992]. The consensus includes either an enhancement or decrease in the magnetic field strength at (or bounding, in the case of crater FTEs) the center of the B_n reversal; an enhancement in the total pressure at the center of FTEs, where the pressure force balances the magnetic tension force [*Ieda et al.*, 1998]; and the presence of a mixture of magnetospheric and magnetosheath plasmas within the FTE structure [e.g., *Klumpar et al.*, 1990], which suggests that FTEs are associated with dayside magnetic reconnection and are important in the coupling between the solar wind and the magnetosphere.

The B_n-reversal signatures and separation time between consecutive FTEs provide clues about the mechanism and dynamics of FTE generation. Various generation hypotheses invoke (1) transient bursts of dayside reconnection [*Russell and Elphic*, 1978], (2) temporal modulation of the reconnection rate during continuous reconnection [*Scholer*, 1988; *Southwood et al.*, 1988; *Phan et al.*, 2004], or (3) multiple X lines (in 2-D representations) or separator lines (in 3-D representations) [e.g., *Lee and Fu*, 1985; *Scholer*, 1995; *Raeder*, 2006; *Hasegawa et al.*, 2010]. These different generation mechanisms necessarily give rise to different magnetic topology or magnetic field connectivity within and around the FTEs. *Fear et al.* [2008] categorized diverse FTE models into three types: the elbow-shaped flux-bundle FTEs, single X line FTEs, and multiple X line FTEs, corresponding to cases 1 to 3, respectively. The elbow-shaped FTEs are postulated to be narrow in dawn-dusk (azimuthal) extent and occur in pairs propagating away from the reconnection site toward the northern/southern magnetic poles. Single X line FTEs featuring the asymmetric B_n reversals can also develop in pairs (north and south of the reconnection site) but can extend azimuthally over long distances. Multiple X line FTEs characterized by distinctly different internal and external signatures can also exhibit large dawn-dusk extent.

Multispacecraft missions have advanced our understanding of the FTE shape, motion, and extent. *Fear et al.* [2008] used tetrahedral Cluster observations to describe an FTE with a much larger azimuthal (dawn-dusk)

than north-south extent, which was inconsistent with the elbow-shaped flux tube model. *Dunlop et al*. [2005] presented Cluster and TC-1 observations of a pair of FTEs propagating northward and southward away from the reconnection site, consistent with the single X line model. *Hasegawa et al*. [2010] reported THEMIS (Time History of Events and Macroscale Interactions during Substorms) observation of an FTE between two converging jets and, therefore, suggested the event formed via multiple X line reconnection [e.g., *Raeder*, 2006]. *Øieroset et al*. [2011] and *Øieroset et al*. [2016] presented similar observations of bidirectional jets converging toward an FTE. Observations of electrons that were not trapped within the core of the event, thus, demonstrated that the FTE was three-dimensional and had an open magnetic field topology rather than the structure of a two-dimensional magnetic island [*Øieroset et al*., 2011]. *Hasegawa et al*. [2016] showed that a mesoscale (peak-to-peak B_n duration of < 1 min) FTE formed during quasi-continuous multiple X line reconnection as indicated by ion flow and Hall magnetic field changes. *Eastwood et al*. [2016] reported ion-scale (~7 ion inertial length radius) FTEs and demagnetized ions observed by Magnetospheric Multiscale mission (MMS).

Theoretical and observational efforts have been made to reveal the substructure of FTEs. *Farrugia et al*. [1987] first separated the region within the FTE open flux tube from its outside boundary layers characterized by draping of magnetic field and plasma flow around the flux tube. *Rijnbeek et al*. [1987] identified a third regime nested between the core and draping regions of the FTE. Observations of energetic electron and ion flows and a magnetic field deflection from its surrounding regions indicate that the third regime contains newly opened magnetic field lines. *Owen et al*. [2001] used Cluster observations to define the magnetic field connectivity inferred from the magnetic field and electron signatures. They resolved sublayers around/within the FTE: a compression region of enhanced field strengths and magnetospheric electrons prior to the leading edge of the FTE, an open flux tube region predominantly filled with magnetosheath electrons on the circulated magnetic fields within the FTE, and a trapping region of magnetospheric electrons on the most recently reconnected flux tubes within the FTE. *Owen et al*. [2008] identified the boundary layer of crater FTEs that features accelerated magnetosheath electrons and injected magnetosheath ions and related the layer to a separatrix region of reconnected flux tubes. *Farrugia et al*. [2011] presented a single X line crater FTE with multiple layers that can be identified on the basis of their magnetic, electric, and plasma signatures. *Varsani et al*. [2014] also investigated the multilayer interior and surrounding structures of a crater FTE based on the electron pitch angles using 125 ms observations of Cluster-PEACE measurements assuming that the electrons were gyrotropic. *Øieroset et al*. [2016] reported evidence for the existence of a reconnecting current sheet at the center of a FTE.

The Magnetospheric Multicale mission (MMS) [*Burch et al*., 2015] was launched on 12 March 2015 and probed Earth's duskside magnetopause for the first time on 15 August 2015. In this paper, we present MMS observations of a single FTE formed under dawnward and southward interplanetary magnetic field (IMF) conditions on 15 August 2015. The four MMS spacecraft in their tetrahedral configuration were separated by an average of ~196 km, which allowed for the investigation of the shape and motion of the FTE. In particular, high-resolution particle and field data facilitate our exploration of FTE substructures and their magnetic connectivity inside and surrounding the FTE.

2. Instrumentation

The four MMS spacecraft fly in highly elliptical equatorial orbits. They are identically equipped with fast plasma investigations (FPI) [*Pollock et al*., 2016], energetic particle detectors (EPD) [*Mauk et al*., 2014], fluxgate magnetometers (FGM consisting of the digital fluxgate magnetometer, DFG, and the analog magnetometer, AFG) [*Russell et al*., 2014], and electric field instruments consisting of the single-plane double probe (SDP) and the axial double probe (ADP) [*Ergun et al*., 2014]. We used the magnetic field data from FGM with a time resolution of 62.5 ms in survey mode, the DC electric field data calibrated from SDP and ADP (with a 31.25 ms time resolution in fast mode), particle data from FPI-DIS (dual ion spectrometers) with a 150 ms time resolution for ions and from FPI-DES (dual electron spectrometers) with a 30 ms time resolution for electrons in burst mode, and high-energy particle data from EPD-EIS (energetic ion spectrometer) with a 0.67 s (2.5 s) time resolution in burst (survey) mode. EPD-EIS obtains a full pitch angle distribution once per spin (20 s).

3. Overview of the Event

During MMS' first encounter with an isolated FTE on 15 August 2015, the barycenter of the MMS quartet was located near the duskside magnetopause southward of the magnetic equator, at [1.3, 9.2, −4.4] Earth radii (R_E).

Figure 1 shows the detailed field and particle signatures from 1325:15 to 1326:20 UT, including the event observed by MMS 3. Figure 1a presents the magnetic field strength (black profiles) together with the x (blue), y (green), and z (red) components of the magnetic field in GSM coordinates. Figure 1b shows the magnetic field components in the LMN boundary coordinate system: B_l (red), B_m (green), and B_n (blue). We determined the LMN coordinates by employing minimum variance analysis (MVA) [*Sonnerup and Scheible*, 1998] using the magnetic field data for the period around the core region of the FTE marked by the vertical cyan dashed lines, "C" at the top of Figure 1, from ~1325:43 to 1325:53 UT: $l = [-0.46, 0.35, 0.82]$, $m = [0.84, -0.13, 0.53]$, $n = [0.29, 0.93, -0.24]$. The medium-to-minimum (maximum-to-medium) eigenvalue ratio is ~26.6 (7.4), indicating a reliable calculation [*Siscoe and Suey*, 1972; *Fear et al*., 2012]. To comply with conventions, m points from postnoon to prenoon along the magnetopause (here mostly sunward), and n points outward from the magnetopause.

Figures 1c and 1d show a time series of the projection of the magnetic field vectors (**B**) and their perturbations ($\mathbf{B} - \overline{\mathbf{B}}$, where $\overline{\mathbf{B}}$ represents the preevent magnetic field averaged over 1325:15–25 UT) onto the MN plane, respectively. Figures 1e and 1f present the electric field components in GSM and LMN coordinates, respectively. The color-coded ion (Figure 1g) and electron (Figure 1h) energy spectrograms, and the pitch angle distributions of the low-energy ($<$100 eV), mid- (100 eV $<$ energy $<$ 1 keV), and high- ($>$1 keV) energy electrons follow (Figures 1i, 1j, and 1k, respectively). Figure 1l shows high-energy (48–210 keV) proton fluxes averaged over six look directions of the EPD-EIS instrument. Figures 1m and 1n (Figures 1o and 1p) present the ion (electron) velocity components in GSM (1m and 1o) and LMN (1n and 1p) coordinates, respectively. The ion and electron number densities (cyan in Figures 1q and 1r) are presented together with the ion/electron total (black), parallel (blue), and perpendicular (red) temperatures. Figure 1s shows the plasma (red) and magnetic (blue) pressures, and the sum of plasma and magnetic pressures (black).

The event occurred under steady IMF orientations due dusk (mostly) and south according to ACE observations ([3.9, 12.7, −6.4] nT in GSM at 1325 UT; not shown). MMS resided mainly on the magnetosheath side during the event, as inferred from the mostly negative B_z (Figure 1a) and enhanced fluxes of magnetosheath ions and electrons with energies of $<$ 1 keV and $<$ 100 eV, respectively (Figures 1g and 1h). At ~1325:47.6 UT (the vertical cyan dashed line, C), MMS 3 observed the maximum magnetic strength (~149 nT) that corresponds primarily to an increase in the negative B_x component (and partially in the negative B_z). Simultaneously, B_y (B_n) changed sign from negative to positive across C. These magnetic variations indicate that MMS 3 traversed the magnetosheath side of a southward moving FTE (see Figure 2b) whose axis is oriented mainly to the azimuthal direction (i.e., antisunward here) and slightly north-south, consistent with the MVA-inferred axis [*Fear et al*., 2012], $-m = [-0.84, 0.13, -0.53]$.

Figure 1c demonstrates the helical magnetic field of the flux rope-type FTE. The magnetic field perturbation vectors (Figure 1d) rotate gradually from $-n$ at the beginning of the event through $-m$ at the center of the FTE (C), and then, to $+n$, in a right-handed manner around the event axis, indicating a positive helicity. Although the field rotation is prominent within the interval bounded by vertical black dashed lines, "B" and "D," from 1325:35.2 to 1325:56.8 UT, the signature initially appears at "A" (~1325:26.6 UT) and continues until "E" (~1326:08.9 UT) (magenta arrows in Figure 1d). Near D (and weakly near B), the helicity changes (slightly alters) due to the draping of the magnetic field around the flux rope. We identify the "B–D" region as the interior of the FTE on the basis of the axial component B_m profiles (Figure 1b) and the "A–B"/"D–E" regions as the inbound/outbound exterior of the FTE on the basis of the magnetic fields draping over the FTE.

Plasma observations (Figures 1g–1l, 1q, and 1r) clearly distinguish between the interior and the exterior of the FTE (details in section 5). The electric field and its strength (Figures 1e and 1f) show patterns symmetric to the magnetic field perturbations. The bipolar change (mostly $-E_l$ to $+E_l$) across C is associated with the magnetic field perturbations as to the overall motion of the FTE (section 4). Ion bulk velocities are antisunward and southward at speeds of ~300 km/s (black profiles in Figures 1m and 1n), which correspond to the local Alfvén speeds (magenta in Figure 1m) at the periphery of the FTE. Electrons in general flow with ions throughout the event, except near the center of the FTE at 1325:48.3–48.5 UT marked by black arrows in Figures 1o and 1p (also denoted by vertical black thin dashed lines, h and h′ at the bottom of Figure 1s). Large electron velocities along $-m$ (~parallel to **B**) and flow reversal (most clearly from $+V_n$ to $-V_n$) coincide with the electric field burst (mainly $-E_n$ to $+E_n$; black arrows in Figures 1e and 1f). Significant deviations between electron and ion bulk velocities at this time give rise to the Hall electric field balancing the measured electric field (not shown).

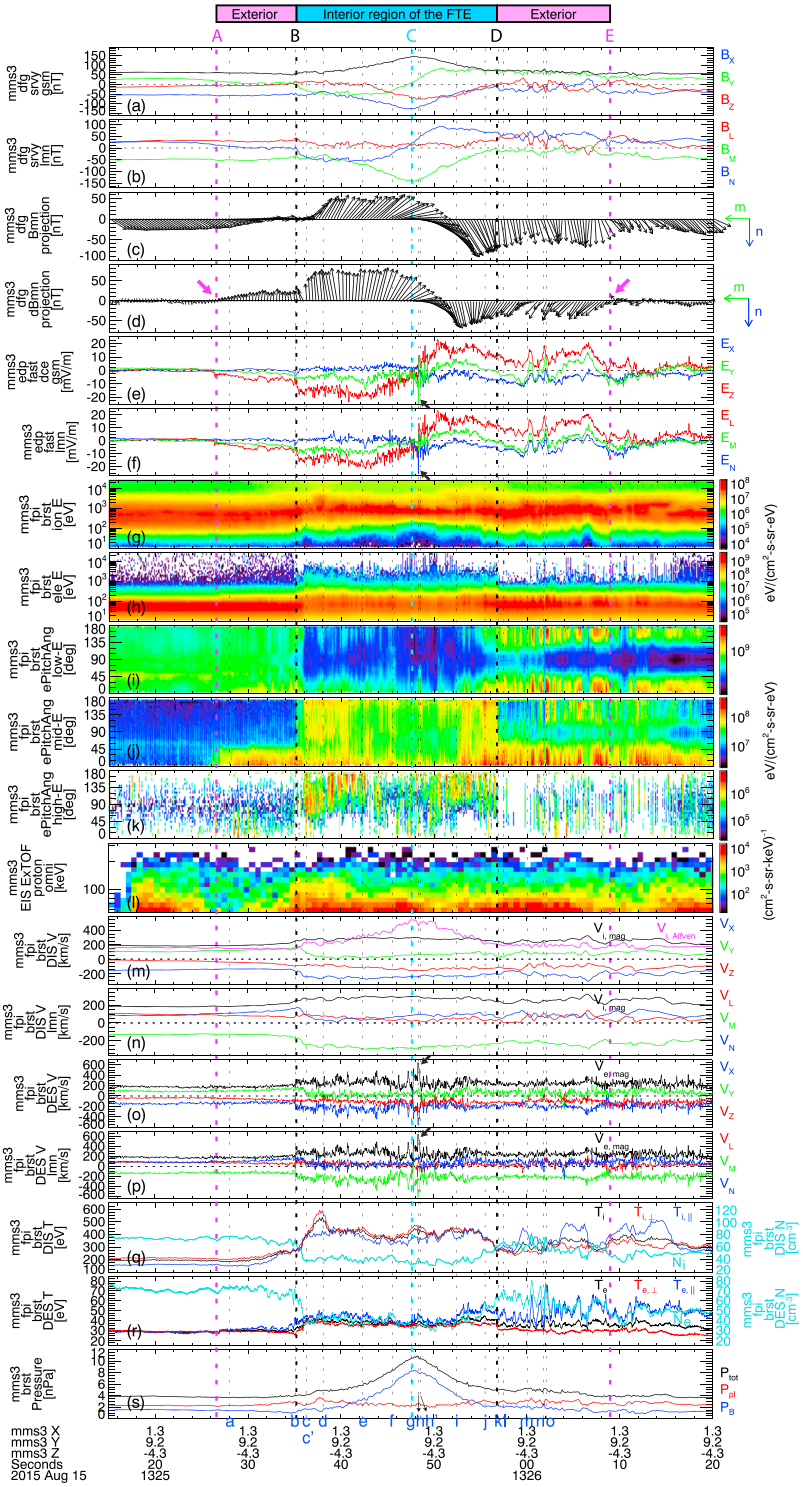

Figure 1. Overview of the FTE crossing by MMS 3: (a and b) the magnetic and (c and f) electric fields in (a and e) GSM and (b and f) LMN coordinates; (c and d) the projection of the magnetic field vectors and their deviations from the preevent level onto the MN plane; (g and h) the ion and electron energy spectrogram; (i–k) the pitch angle distribution of the low-energy (<100 eV), mid- (100 eV < energy < 1 keV), and high- (>1 keV) energy electrons; (l) the spectrogram of high-energy (48–210 keV) proton fluxes averaged over six look directions of the EPD-EIS instrument; (m and n) the ion bulk velocity in GSM and LMN; (o and p) the electron bulk velocity in GSM and LMN; (q and r) the ion and electron number densities (cyan) and the ion/electron total (black), parallel (blue), and perpendicular (red) temperatures; (s) the plasma (red) and magnetic (blue) pressures, and the sum of plasma and magnetic pressures (black).

(a)

	Boundary	Observation time	MVA normal vector	$\lambda_{mid}/\lambda_{min}$ ratio	Propagation velocity
A	Exterior inbound	~1325:26.6 UT	[-0.86, -0.43, 0.25]	7.51	101.5 km/s x [-0.49, -0.20, 0.82]
B	Interior inbound	~1325:35.2 UT	[-0.94, 0.28, 0.15]	5.33	116.0 km/s x [-0.75, -0.62, 0.21]
C	FTE core	~1325:47.6 UT	[-1.00, 0.03, 0.04]	14.6	154.2 km/s x [-0.80, -0.58, 0.14]
D	Interior outbound	~1325:56.8 UT	[0.68, -0.05, 0.76]	6.35	161.1 km/s x [-0.70, -0.71, -0.08]
E	Exterior outbound	~1326:08.9 UT	[0.56, -0.08, 0.85]	2.07	101.1 km/s x [-0.62, -0.64, -0.44]

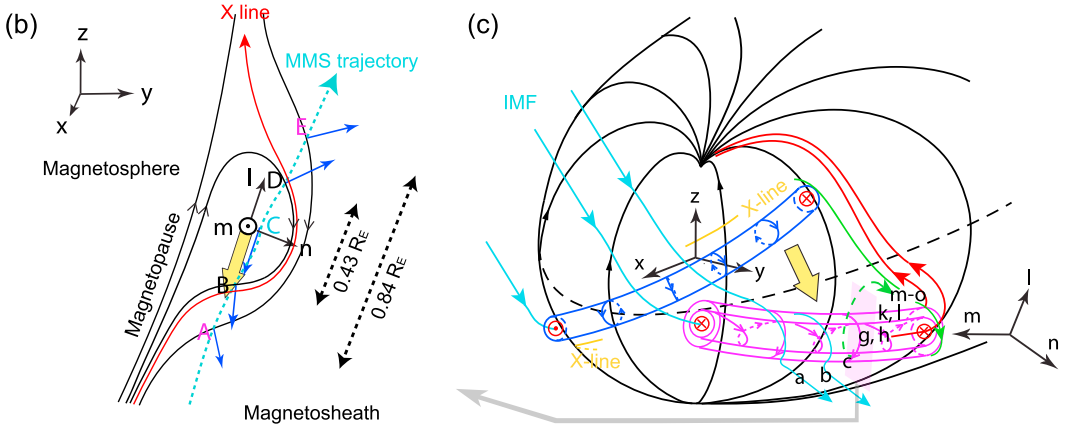

Figure 2. (a) A list of the local boundary normals determined from minimum variance analysis using the magnetic field; the medium-to-minimum eigenvalue ratio averaged over spacecraft; the normal propagation velocities obtained from four-spacecraft timing analysis on each of A to E crossings. (b) An illustration of the cross section of the FTE interior and surrounding region. Blue arrows represent the projections of MVA normal onto the cross section (LN plane). A cyan dashed arrow denotes a possible MMS trajectory. (c) A simplified sketch illustrating the magnetopause on which the FTE (a blue FTE) formed at the northern postnoon and the southern prenoon magnetopause under the duskward and slightly southward IMF propagates toward the low-latitude magnetopause (a magenta FTE). Possible magnetic topology and connectivity to the northern magnetosphere are shown as colored arrows. A magenta shade represents the cross section in Figure 2b. Letters a, b, c, g, h, k, l, and m–o across the magenta FTE represent an MMS passage of the substructure of the FTE and correspond to the times denoted by vertical black thin dashed lines and letters shown at the bottom of Figure 1s.

At the FTE center C, electron bulk speed and plasma densities reach local minimums (Figures 1o–1r). The total pressure peaks at the core of the flux rope [*Paschmann et al.*, 1982] (Figure 1s). Therefore, the pressure force (radially outward from the FTE core) can balance the (inward) magnetic tension force for the steady state flux rope. The current density (calculated from FPI plasma moments) parallel to **B** dominates at the center of the FTE ($J_{||}$, mainly $-J_m = 920\,\mathrm{nA/m^2}$; $J_\perp \sim 100\,\mathrm{nA/m^2}$; not shown), suggestive of a nearly force free FTE ($\mathbf{J}\times\mathbf{B}=0$).

4. Propagation, Shape, and Extent of the FTE

The four MMS spacecraft with an average separation of ~196 km were almost in a tetrahedron enabling us to determine the normal propagation velocity of 2-D planar boundaries via timing analysis [*Paschmann and Daly*, 1998]. To delineate the structure and motion of the FTE, we performed a four-spacecraft timing analysis and magnetic field MVA on each of A to E boundary crossings. Figure 2a lists the normal propagation velocities and the MVA-derived boundary normals in LMN coordinates together with the medium-to-minimum eigenvalue ratio averaged over spacecraft. The directions of MVA normals, which have a 180° ambiguity, are forced to point away from the FTE core. Their projections onto the LN plane (blue arrows in Figure 2b) indicate that MMS entered the bottom of the FTE and exited the (more magnetosheath) topside. This MMS trajectory in the LN plane (the cyan dashed arrow in Figure 2b) is consistent with the FTE propagation mostly along $-l$ (yellow solid arrows in Figures 2b and 2c). The normal and propagation vector somewhat differ, in particular, on crossing D, suggesting a nonplanar or nonsteady state local boundary. The transverse (in the LN plane) scale sizes of the FTE and its surrounding bulge caused by draping magnetic fields inferred from the propagation velocity and durations of their passage past MMS are 0.43 R_E and 0.84 R_E (76.2 d_i, and 150 d_i, respectively, where d_i is the ion inertial length, ~35.7 km, averaged over the period between B and D in Figure 1).

Figure 1l shows high-energy (48–210 keV) proton bursts that occurred in conjunction with the FTE. Pitch angle distributions (not shown) featuring more field-aligned energetic protons with 0–90° pitch angles

provide further evidence for a (mainly) southward moving FTE being pushed southward by reconnection jets emanating from an X line north of the event (Figure 2b). The high-energy protons produced during the reconnection process flow along the reconnected magnetosheath field lines, enhancing parallel fluxes. According to the component reconnection model, the duskward and slightly southward IMF during the event should have facilitated reconnection along a line running from the northern postnoon to the southern prenoon magnetopause (see yellow solid and dashed lines in Figure 2c). A pair of flux ropes (or a long single FTE; see the blue FTE in Figure 2c) can form connected to the northern and southern cusps. They initially propagate toward the equatorial plane at the Alfvén velocity. Combined with the magnetosheath flow velocity, the northern flux rope will drift southward and antisunward along the magnetopause (see the magenta FTE in Figure 2c). The observed FTE motion is consistent with the prediction of *Cooling et al*. [2001]. The proton bursts continued after the FTE interval until ~1328 UT (not shown), indicating ongoing reconnection on the northern postnoon magnetopause and magnetic connectivity to the Northern Hemisphere.

5. Magnetic Topology and Substructure of the FTE

Figures 1g–1k show that particle observations differ in the regions interior and exterior to the FTE. In the interior, enhanced fluxes of >1 keV ions and >100 eV electrons together with reductions in $<$~300 eV ion and $<$~30 eV electron fluxes (Figures 1g and 1h) lead to lower plasma densities and larger temperatures (Figures 1q and 1r) than exterior to the FTE. Electron pitch angle distributions inside the FTE are energy dependent: low- (mid and high) energy electrons are mostly parallel (bidirectional and antiparallel) streaming (Figures 1i–1k). Electrons of magnetosheath (low energy) and magnetospheric (high energy) origin, therefore, counterstream, indicating an open magnetic topology within the flux rope whose core is magnetically connected to the northern magnetosphere. The bidirectional midenergy electrons suggest the coexistence of particles entering and subsequently being mirrored from the northern ionosphere. The two exterior regions (A–B and D–E) of the FTE differ in plasma properties. At the entrance (A–B), the electrons exhibit two populations: pristine magnetosheath electrons that are mostly isotropic (Figure 1i) and heated magnetosheath electrons that are parallel streaming (Figure 1j). The pristine isotropic magnetosheath electrons are absent from the exit exterior (D–E) where bidirectional (mostly parallel) low (mid)-energy electrons dominate.

Figures 3a and 3d show 2-D cuts of 3-D ion and electron distributions with a 150 ms and 30 ms time resolution, respectively, at selected times denoted by "a" to "o" at the bottom of Figure 1s. The parallel axis of these ($V_{||}$, $V_{\perp}$) distributions represents the direction in a 3-D velocity space along the local magnetic field (**B**). The perpendicular direction is chosen to be perpendicular to **B** and approximately along the ion bulk velocity (**V**), $\mathbf{V}_{\perp} = \mathbf{B} \times (\mathbf{V} \times \mathbf{B})$.

5.1. Inbound Exterior

At a inside the outer boundary A, the bulk magnetosheath ions (Figure 3Aa) flow along the magnetic field and show a greater spread in $V_{\perp}$ than $V_{||}$, indicating a temperature anisotropy ($T_{i,\perp} > T_{i,||}$; Figure 1q). Pristine magnetosheath electrons (Figure 3Da) are cold and isotropic. The distribution is superposed by the heated magnetosheath electrons streaming along **B** (red arrow in Figure 3Da), which persist until prior to entering the FTE (red arrow in Figure 3Db). These particles may have leaked from the flux rope and flow along the draping magnetosheath field lines (see the cyan field line wrapping around the magenta FTE in Figure 2c).

5.2. Exterior-Interior Interfaces

Near two inner boundaries B and D separating the exterior regions from the interior FTE (at "b," "k," and "l"), the parallel motion of bulk ions still exists but core populations exhibit dominant injections transverse to **B** (red arrows in Figures 3Ab, 3Ak, and 3Al). At those times, bulk electrons develop a bullet-shaped distribution ($T_{e,||} > T_{e,\perp}$) that is asymmetric around $V_{||} = 0$ (Figures 3Db, 3Dk, and 3Dl). They display antiparallel ($-V_{||}$) enhancements of electrons streaming against the magnetic field, i.e., toward the X line north of the FTE (see Figure 2b). On the other hand, the heated populations (red arrows) appear with pitch angles around 0°, i.e., emanating from the X line.

A combination of these observations is consistent with past observations and simulations of reconnection separatrix crossings. Ions moving along **B** and electrons moving against the field are responsible for the Hall current and fields featuring separatrices, as pointed out by *Farrugia et al*. [2011]. Ion distributions show an excellent agreement with Figure 14 of *Farrugia et al*. [2011] describing the core-draping interface that

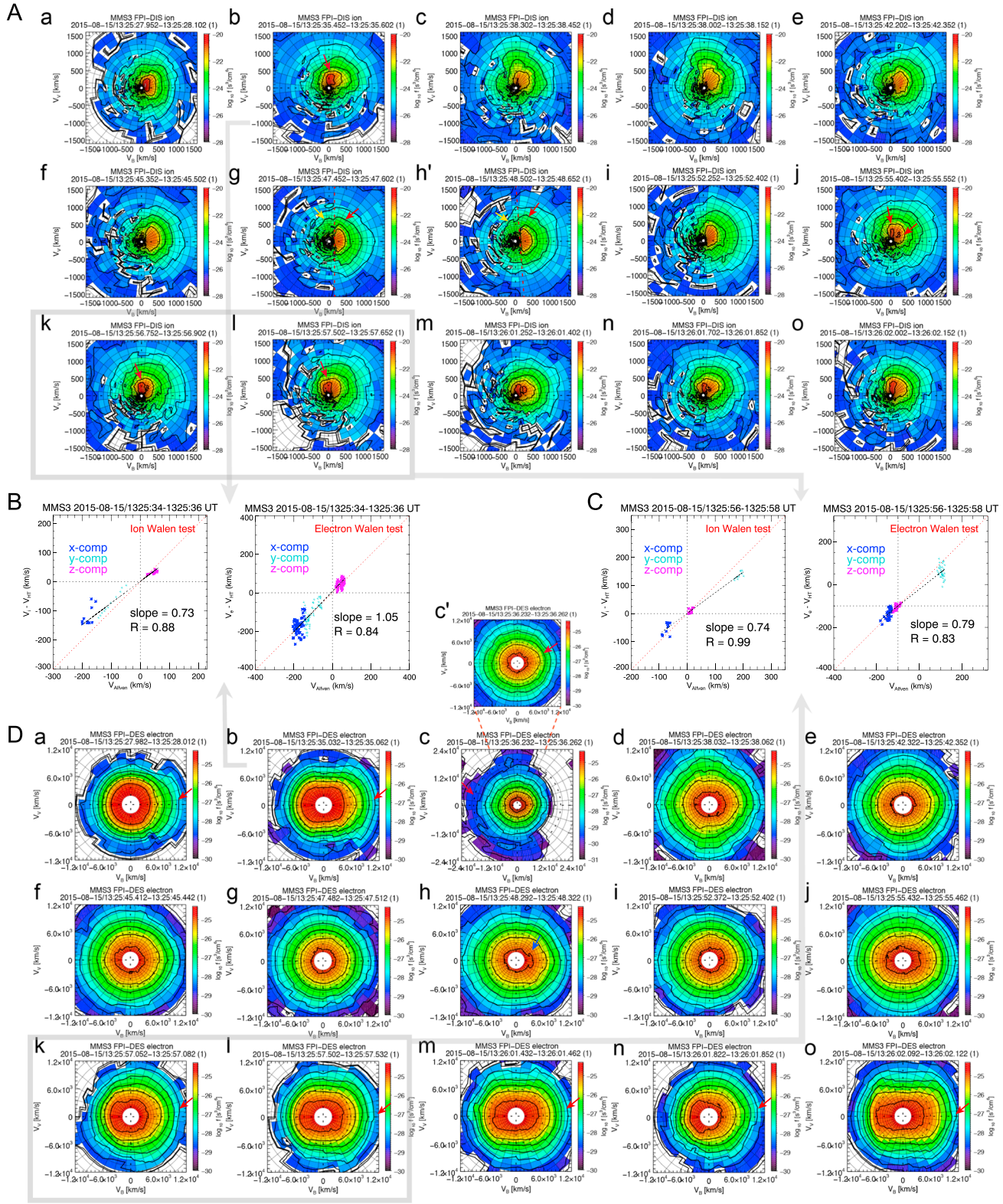

Figure 3. (A and D) Ion and electron ($V_{||}$, $V_{\perp}$) distributions measured by FPI-DIS and DES with a 150 ms and 30 ms time resolution at selected times, denoted by a to o at the bottom of Figure 1s. The parallel axis of these ($V_{||}$, $V_{\perp}$) distributions represents the direction along the local magnetic field (**B**). The perpendicular direction is chosen to be perpendicular to **B** and approximately along the ion bulk velocity (**V**), $\mathbf{V}_{\perp} = \mathbf{B} \times (\mathbf{V} \times \mathbf{B})$. (B and C) Ion (left) and electron (right) Walén tests for MMS3 passage of the inbound (Figure 3B) and outbound (Figure 3C) interface between the exterior and interior regions. The inbound interface-crossing period includes the time when distribution b is sampled. The outbound period includes the times selected for distributions k and l.

includes a separatrix. Kinetic simulations [*Egedal et al*., 2005, 2008, 2013] predicted that as the electrons move toward the Hall region across the separatrix, they undergo reflection either off a field-aligned potential boundary or at a mirror point surrounding a region of weak magnetic field. *Hwang et al*. [2013] pointed out that the difference in electron fluxes into and out of an X line along the separatrix, or reflection of a portion of the initial electron beam flowing into an X line, could cause such asymmetry.

Motivated by this observation, we performed a Walén test in the de Hoffmann-Teller frame separately for ions and electrons on B and D crossings (Figures 3b and 3c). The Walén test identifies a current sheet layer undergoing reconnection as rotational discontinuities. We used the generalized Walén relation formula, adopted from equation (32) of *Scudder et al*. [1999] that takes into account the pressure anisotropy. At both boundaries, the ions and electrons (left and right panels of Figures 3b and 3c) do satisfy the Walén test exhibiting a slope close to 1, as expected for current sheets undergoing reconnection. This provides further evidence that the exterior-interior interface is likely to contain a separatrix connected to an X line.

5.3. Interior

In the interior (B–D; distributions c–j in Figures 3A and 3D) electrons display more isotropic distributions than exterior to the FTE; ions develop a clearer D-shaped distribution function toward the center of the FTE. Immediately inside the FTE the high-energy electrons of magnetosphere origin appear with pitch angles around 180° (red arrow in Figure 3Dc). Simultaneously, the heated electrons of magnetosheath origin coexist along **B** (red arrow in Figure 3Dc′). Ions (Figure 3Ac) show a large spread in $+V_{\perp}$, leading to a temperature anisotropy ($T_{i,\perp} > T_{i,||}$), which peaks at "d" (Figure 3Ad). Accordingly, perpendicular-heated electrons combined with parallel-heated low-energy components form a diamond-shape distribution (Figure 3Dd).

The central region of the FTE exhibits a mixture of such low- and high-energy plasmas with different origin (distributions e–i). Open magnetic field topologies, for example, the magnetosheath magnetic field line entering into the leftside cross section of the magenta FTE and exiting from the rightside cross section and to connect to the Northern Hemisphere (illustrated in Figure 2c) explains the coexistence and mixture of electrons.

At/around the axis of flux ropes (1325:46.102–50.302 UT; in particular, Figure 3Ah′), accelerated magnetosheath ions demonstrate D-shaped distributions with a cutoff (red dashed lines in Figures 3Ag and 3Ah′) at $V_{||} = \sim 150$ km/s. This cutoff, predicted to represent the de Hoffmann-Teller frame velocity [*Cowley*, 1995], bisects incident and reflected particles (red and yellow arrows in Figures 3Ag and 3Ah′). Unlike the theoretical prediction, the HT velocity parallel to **B** is estimated to be 259 km/s. This suggests that the magnetic field at the core FTE (~at C) is *old* reconnected field lines, contrary to the separatrix (embedded within B and D) on *newly* opened field lines.

Heated isotropic magnetosheath electrons populate the core flux ropes (Figure 3Dg) and lead to a local minimum in density and flux, similar to previous observations [*Varsani et al*., 2014]. Figure 3Dh shows a disturbed distribution in coincidence with the electric field burst described in section 3 (black arrows in Figures 1e and 1f). Before exiting the FTE, ions show a mixture of transverse and parallel core populations (red arrows in Figure 3Aj) and bidirectional electrons start to form a bullet-shaped distribution (Figure 3Dj).

5.4. Outbound Exterior

In the outbound exterior region (D–E; distributions m–o), a perpendicular-injecting core and parallel-streaming ions coexist. The loss of high-energy electrons and bullet-shaped distributions with counterstreaming (more antiparallel) low-energy electrons is notable. Low-energy magnetosheath electrons traveling along the draped fields that enclose the lower flux rope (see the green arrow around the magenta FTE in Figure 2c) may be reflected back due to an increasing magnetic strength closer to the flux rope, which results in the bullet-shaped distribution. Another interpretation is that the draped fields may involve magnetic fields that are entrained with the inflow jets toward the reconnection site above the FTE. Electrons on those field lines are often counterstreaming [e.g., *Chen et al*., 2008; *Hwang et al*., 2013].

Ion and electron distributions within this region (D–E) change rapidly along the MMS trajectory (e.g., Figure 3 Do compared with Figure 3Dn, ~0.17 s later), indicating multiple layers of draped magnetic fields with different connectivities to the magnetosphere and the FTE. On the other hand, accelerated magnetosheath electrons (red arrows in Figures 3Dm–3Do) persist in the parallel ($+V_{||}$) direction. That is, they flow along the

draped fields that emerge either from the reconnection site north of the FTE or from the lower flux rope (the green dashed arrow in Figure 2c). Throughout the inbound and outbound exterior regions (A–B and D–E), the accelerated population appears unidirectional ($+V_{||}$). This indicates that single X line reconnection located north of the observation point was operating during the event or responsible for the generation of the FTE, which is incorporated in Figure 2b.

6. Summary

The paper presents a flux rope observed on the duskside magnetopause by MMS. The combined field and particle observations indicate that the FTE likely formed on the northern postnoon magnetopause and then propagated southward/antisunward. The transverse scale sizes of the FTE and its surrounding bulge caused by draping magnetic fields are inferred to be 0.43 R_E and 0.84 R_E, respectively. We use the high time resolution FPI distributions to explore the magnetic topologies inside and outside the FTE. The core fields are open, magnetically connected to the northern magnetosphere from which high-energy electrons (enhanced at 180° pitch angle) emerge. D-shaped ion distributions and isotropic distributions of heated magnetosheath electrons characterize the axis of flux ropes that carry old-opened field lines. Plasma densities and electron number flux reach a local minimum at the center. Counterstreaming electrons superposed by heated magnetosheath electrons leaving from the FTE or from the reconnection site north of the FTE populate the exterior region surrounding the FTE. Unidirectional high-energy electrons throughout the entrance and exit exterior crossings indicate a single X line reconnection model explaining the formation of the FTE. High time resolution ion and electron distributions suggest the existence of a thin layer (at the interface between the interior and exterior to the FTE) containing a separatrix of newly opened magnetic field lines that emanate from the X line above the FTE. The present event, via the investigation of the highest-ever-achieved time resolution particle distributions, suggests multiple layers of both open and draped magnetic fields with rapid-varying connectivities to the magnetosphere and the FTE.

Acknowledgments

This study was supported, in part, by NASA's MMS project at the Goddard Space Flight Center with data from MMS. MMS data sets were provided by the MMS science working group teams through the link (http://lasp.colorado.edu/mms/sdc/public/). We acknowledge MMS FPI (Thomas E. Moore, Yoshifumi Saito, Jean-Andre Sauvaud, Victoria Coffey, Benoit Lavraud, Michael Chandler, and Conrad Schiff), Fields and EPD teams for providing data. K.J.H. thanks members of the MMS Modeling/Theory team for useful discussions.

References

Burch, J. L., T. E. Moore, R. B. Torbert, and B. L. Giles (2015), Magnetospheric multiscale overview and science objectives, *Space Sci. Rev.*, doi:10.1007/s11214-015-0164-9.

Chen, L.-J., et al. (2008), Evidence of an extended electron current sheet and its neighboring magnetic island during magnetotail reconnection, *J. Geophys. Res.*, *113*, A12213, doi:10.1029/2008JA013385.

Cooling, B. M. A., C. J. Owen, and S. J. Schwartz (2001), Role of the magnetosheath flow in determining the motion of open flux tubes, *J. Geophys. Res.*, *106*, 18,763–18,776, doi:10.1029/2000JA000455.

Cowley, S. W. H. (1995), Theoretical perspectives of the magnetopause: A tutorial review, in *Physics of the Magnetopause*, edited by P. Song, B. U. Ö. Sonnerup, and M. F. Thomsen, pp. 29–43, AGU, Washington, D. C., doi:10.1029/GM090p0029.

Dunlop, M. W., et al. (2005), Coordinated Cluster/Double Star observations of dayside reconnection signatures, *Ann. Geophys.*, *23*, 2867–2875, doi:10.5194/angeo-23-2867-2005.

Eastwood, J. P., et al. (2016), Ion-scale secondary flux ropes generated by magnetopause reconnection as resolved by MMS, *Geophys. Res. Lett.*, *43*, 4716–4724, doi:10.1002/2016GL068747.

Egedal, J., M. Øieroset, W. Fox, and R. P. Lin (2005), In situ discovery of an electrostatic potential, trapping electrons and mediating fast reconnection in the Earth's magnetotail, *Phys. Rev. Lett.*, *94*, 025006, doi:10.1103/PhysRevLett.94.025006.

Egedal, J., W. Fox, M. Porkolab, M. Øieroset, R. P. Lin, W. Daughton, and J. F. Drake (2008), Evidence and theory for trapped electrons in guide field magnetotail reconnection, *J. Geophys. Res.*, *113*, A12207, doi:10.1029/2008JA013520.

Egedal, J., A. Le, and W. Daughton (2013), A review of pressure anisotropy caused by electron trapping in collisionless plasma, and its implications for magnetic reconnection, *Phys. Plasmas*, *20*, 18, doi:10.1063/1.4811092.

Ergun, R. E., et al. (2014), The axial double probe and fields signal processing for the MMS mission, *Space Sci. Rev.*, doi:10.1007/s11214-014-0115-x.

Farrugia, C. J., R. C. Elphic, D. J. Southwood, and S. W. H. Cowley (1987), Field and flow perturbations outside the reconnected field line region in flux transfer events: Theory, *Planet. Space Sci.*, *35*, 227–240.

Farrugia, C. J., et al. (2011), "Crater" flux transfer events: Highroad to the X line?, *J. Geophys. Res.*, *116*, A02204, doi:10.1029/2010JA015495.

Fear, R. C., S. E. Milan, A. N. Fazakerley, E. A. Lucek, S. W. H. Cowley, and I. Dandouras (2008), The azimuthal extent of three flux transfer events, *Ann. Geophys.*, *26*, 2353–2369, doi:10.5194/angeo-26-2353-2008.

Fear, R. C., S. E. Milan, and K. Oksavik (2012), Determining the axial direction of high-shear flux transfer events: Implications for models of FTE structure, *J. Geophys. Res.*, *117*, A09220, doi:10.1029/2012JA17831.

Hasegawa, H., et al. (2010), Evidence for a flux transfer event generated by multiple X-line reconnection at the magnetopause, *Geophys. Res. Lett.*, *37*, L16101, doi:10.1029/2010GL044219.

Hasegawa, H., et al. (2016), Decay of mesoscale flux transfer events during quasi-continuous spatially extended reconnection at the magnetopause, *Geophys. Res. Lett.*, *43*, 4755–4762, doi:10.1002/2016GL069225.

Hwang, K.-J., M. L. Goldstein, D. E. Wendel, A. N. Fazakerley, and C. Gurgiolo (2013), Cluster observations near reconnection X-lines in Earth's magnetotail current sheet, *J. Geophys. Res. Space Physics*, *118*, 4199–4209, doi:10.1002/jgra.50403.

Ieda, A., S. Machida, T. Mukai, Y. Saito, T. Yamamoto, A. Nishida, T. Terasawa, and S. Kokubun (1998), Statistical analysis of plasmoid evolution with GEOTAIL observations, *J. Geophys. Res.*, *103*, 4453–4465, doi:10.1029/97JA03240.

Kawano, H., S. Kokubun, and K. Takahashi (1992), Survey of transient magnetic field events in the dayside magnetosphere, *J. Geophys. Res.*, *97*, 10,677–10,692, doi:10.1029/92JA00369.

Klumpar, D. M., S. A. Fuselier, and E. G. Shelley (1990), Ion composition measurements within magnetospheric flux transfer events, *Geophys. Res. Lett.*, *17*, 2305–2308, doi:10.1029/GL017i013p02305.

Lee, L. C., and Z. F. Fu (1985), A theory of magnetic flux transfer at the Earth's magnetopause, *Geophys. Res. Lett.*, *12*, 105–108, doi:10.1029/GL012i002p00105.

Mauk, B. H., et al. (2014), The Energetic Particle Detector (EPD) Investigation and the Energetic Ion Spectrometer (EIS) for the Magnetospheric Multiscale (MMS) mission, *Space Sci. Rev.*, doi:10.1007/s11214-014-0055-5.

Øieroset, M., et al. (2011), Direct evidence for a three-dimensional magnetic flux rope flanked by two active magnetic reconnection X-lines at Earth's magnetopause, *Phys. Rev. Lett.*, *107*, 165007, doi:10.1103/PhysRevLett.107.165007.

Øieroset, M., et al. (2016), MMS observations of large guide field symmetric reconnection between colliding reconnection jets at the center of a magnetic flux rope at the magnetopause, *Geophys. Res. Lett.*, *43*, 5536–5544, doi:10.1002/2016GL069166.

Owen, C. J., et al. (2001), Cluster PEACE observations of electrons during magnetospheric flux transfer events, *Ann. Geophys.*, *19*, 1509–1522, doi:10.5194/angeo-19-1509-2001.

Owen, C. J., A. Marchaudon, M. W. Dunlop, A. N. Fazakerley, J. M. Bosqued, J. P. Dewhurst, R. C. Fear, S. A. Fuselier, A. Balogh, and H. Rème (2008), Cluster observations of "crater" flux transfer events at the dayside high-latitude magnetopause, *J. Geophys. Res.*, *113*, A07S04, doi:10.1029/2007JA012701.

Paschmann, G., and P. W. Daly (1998), *Analysis Methods for Multispacecraft Data*, *Sci. Rep. 001*, Int. Space Sci. Inst., Bern.

Paschmann, G., G. Haerendel, I. Papamastorakis, N. Sckopke, S. J. Bame, J. T. Gosling, and C. T. Russell (1982), Plasma and magnetic-field characteristics of magnetic-flux transfer events, *J. Geophys. Res.*, *87*, 2159–2168, doi:10.1029/JA087iA04p02159.

Phan, T. D., et al. (2004), Cluster observations of continuous reconnection at the magnetopause under steady interplanetary magnetic field conditions, *Ann. Geophys.*, *22*, 2355–2367.

Pollock, C., et al. (2016), Fast Plasma Investigation for Magnetospheric Multiscale, *Space Sci. Rev.*, doi:10.1007/s11214-016-0245-4.

Raeder, J. (2006), Flux transfer events: 1. Generation mechanism for strong southward IMF, *Ann. Geophys.*, *24*, 381–392.

Rijnbeek, R. P., C. J. Farrugia, D. J. Southwood, M. W. Dunlop, W. A. C. Mier-Jedrzejowicz, C. P. Chaloner, D. S. Hall, and M. F. Smith (1987), A magnetic boundary signature within flux transfer events, *Planet. Space Sci.*, *35*, 871–878.

Russell, C. T., and R. C. Elphic (1978), Initial ISEE magnetometer results—Magnetopause observations, *Space Sci. Rev.*, *22*, 681–715, doi:10.1007/BF00212619.

Russell, C. T., et al. (2014), The Magnetospheric Multiscale Magnetometers, *Space Sci. Rev.*, doi:10.1007/s11214-014-0057-3.

Scholer, M. (1988), Magnetic flux transfer at the magnetopause based on single X-line bursty reconnection, *Geophys. Res. Lett.*, *15*, 291–294, doi:10.1029/GL015i004p00291.

Scholer, M. (1995), Models of flux transfer events, in *Physics of the Magnetopause*, *Geophys. Monogr. Ser.*, vol. 90, edited by P. Song, B. U. Ö. Sonnerup, and M. F. Thomsen, pp. 235–245, AGU, Washington, D. C.

Scudder, J. D., P. A. Puhl-Quinn, F. S. Mozer, K. W. Ogilvie, and C. T. Russell (1999), Generalized Walén tests through Alfvén waves and rotational discontinuities using electron flow velocities, *J. Geophys. Res.*, *104*, 19,817–19,834, doi:10.1029/1999JA900146.

Sibeck, D. G., and G. L. Siscoe (1984), Downstream properties of magnetic flux transfer events, *J. Geophys. Res.*, *89*, 10,709–10,715, doi:10.1029/JA089iA12p10709.

Siscoe, G. L., and R. W. Suey (1972), Significance criteria for variance matrix applications, *J. Geophys. Res.*, *77*, 1321–1322, doi:10.1029/JA077i007p01321.

Sonnerup, B. U. Ö., and M. Scheible (1998), Minimum and maximum variance analysis, in *Analysis Methods for Multi-Spacecraft Data*, edited by G. Paschmann and P. W. Daly chap. 8, pp. 185–220, ESA Publ., Noordwijk, Netherlands.

Southwood, D. J., M. A. Saunders, M. W. Dunlop, W. A. C. Mierjedrzejowicz, and R. P. Rijnbeek (1986), A survey of flux transfer events recorded by the UKS spacecraft magnetometer, *Planet. Space Sci.*, *34*, 1349–1359.

Southwood, D. J., C. J. Farrugia, and M. A. Saunders (1988), What are flux transfer events?, *Planet. Space Sci.*, *36*, 503–508.

Varsani, A., et al. (2014), Cluster observations of the substructure of a flux transfer event: Analysis of high-time-resolution particle data, *Ann. Geophys.*, *32*, 1093–1117, doi:10.5194/angeo-32-1093-2014.